

Greatly enhanced fatigue resistance in $\text{Hf}_{0.5}\text{Zr}_{0.5}\text{O}_2/\text{La}_{0.7}\text{Sr}_{0.3}\text{MnO}_3$ superlattices

Peijie Jiao,¹ Zhiyu Liu¹, Hongying Chen,¹ Mingkai Qing,¹ Yurong Yang,¹ Yu Deng,^{1,*} and Di Wu^{1,2,†}

¹*National Laboratory of Solid State Microstructures, Department of Materials Science and Engineering, Jiangsu Key Laboratory of Artificial Functional Materials, and Collaborative Innovation Center of Advanced Microstructures, Nanjing University, Nanjing 210093, China*

²*School of Materials Science and Intelligent Engineering, Nanjing University, Suzhou 215163, China*

(Received 22 October 2023; revised 6 February 2024; accepted 24 April 2024; published 10 May 2024)

Superlattices composed of $\text{Hf}_{0.5}\text{Zr}_{0.5}\text{O}_2/\text{La}_{0.7}\text{Sr}_{0.3}\text{MnO}_3$ (HZO/LSMO), with nominally 10-nm-thick HZO and 1-nm-thick LSMO in a period, were deposited epitaxially on (110)-oriented $(\text{La}_{0.3}\text{Sr}_{0.7})(\text{Al}_{0.65}\text{Ta}_{0.35})\text{O}_3$ (LSAT) substrates with thick LSMO electrodes. These 1-nm-thick LSMO spacer layers interrupt the growth of HZO grains, keeping the superlattice free from a paraelectric monoclinic phase. This makes it possible to achieve a total superlattice thickness above 50 nm in the pure ferroelectric orthorhombic phase. The strain gradient due to the strain relaxation in thick superlattices induces a rhombohedral distortion with the help of the flexoelectric field. The distorted structure is more stable than the metastable orthorhombic ferroelectric phase, making it more resistant to ferroelectric fatigue. The $(\text{HZO}/\text{LSMO})_5$ superlattice exhibits a large remanent polarization of about $19.3 \mu\text{C}/\text{cm}^2$ and a greatly enhanced fatigue resistance, by keeping more than 90% of its polarization after 10^9 bipolar switching cycles. Our results provide additional opportunities for the design and optimization of HfO_2 -based ferroelectric materials to optimize the structure and properties for integrated ferroelectric applications.

DOI: 10.1103/PhysRevApplied.21.054024

I. INTRODUCTION

Since the first discovery of ferroelectricity in Si-doped HfO_2 thin films in 2011, HfO_2 -based ferroelectric thin films have attracted increasing interest from both academia and industry [1]. Due to the robust ferroelectric properties observed at reduced dimensions [2], fast domain switching [3], and, most importantly, the compatibility with complementary metal-oxide-semiconductor processes [4,5], these HfO_2 -based thin films have shown tremendous potential for applications in ferroelectric random access memories, negative capacitance transistors, ferroelectric tunnel junctions, and neuromorphic devices [5–9].

The compound HfO_2 in bulk has a high-symmetry cubic phase above 2773 K, in a tetragonal (*t*) phase between 1937 and 2773 K, and in a monoclinic (*m*) phase below 1937 K [10]. Although all the cubic, *t*-, and *m*-phases are nonpolar, metastable polar orthorhombic (*o*) or rhombohedral (*r*) HfO_2 may be stabilized at room temperature, cooling from the nonpolar *t*-phase under certain chemical and elastic boundary conditions [11–13]. Following the seminal work on Si-doped HfO_2 , various dopants have been

reported to induce ferroelectricity in HfO_2 -based films deposited by various techniques [14–18]. Among these doped- HfO_2 films, $\text{Hf}_{0.5}\text{Zr}_{0.5}\text{O}_2$ (HZO) has shown the most robust ferroelectric properties and has been studied most intensively [8–10]. Most of the HZO films reported were polycrystalline, composed of ferroelectric *o*-phase with centrosymmetric *t*- and *m*-phases that make it difficult to understand the ferroelectricity in metastable HfO_2 -based thin films [19,20]. Recently, it has been demonstrated that the ferroelectric *o*- and *r*-phases can be widely stabilized in epitaxial HZO films grown on perovskite substrates [21–25]. However, it is well-known that there is a phase transition from the metastable phases into the thermodynamically stable nonpolar *m*-phase since the mismatch strain relaxes with increasing film thickness [26]. To date, phase-pure epitaxial HZO ferroelectric thin films are not thicker than 10 nm [21]. It is desirable to suppress the *m*-phase for improved understanding and optimized ferroelectric properties.

In this paper, we report the stabilization of *r*-distorted ferroelectric *o*-phase free from the nonpolar *m*-phase up to at least 50 nm in total thickness by constructing HZO/ $\text{La}_{0.7}\text{Sr}_{0.3}\text{MnO}_3$ (HZO/LSMO) superlattices on (110)-oriented $(\text{La}_{0.3}\text{Sr}_{0.7})(\text{Al}_{0.65}\text{Ta}_{0.35})\text{O}_3$ (LSAT) substrates. The reason that LSAT substrates are chosen is that

*Corresponding author: dengyu@nju.edu.cn

†Corresponding author: diwu@nju.edu.cn

the HZO films we deposited on the (110)-oriented LSAT substrates show better crystallographic quality compared with those we deposited on (110)-oriented STO substrates [27]. Greatly enhanced fatigue resistance in the superlattices was observed due to the *r*-distorted ferroelectric phase, which is energetically more stable than the *o*-phase in the absence of distortion.

II. EXPERIMENT

The 20-nm-thick LSMO electrode, the HZO single layers, and the HZO/LSMO superlattices, with 10-nm-thick HZO and 1-nm-thick LSMO in a period, were deposited on (110)-oriented LSAT single-crystalline substrates by pulsed laser deposition (AdNano Corp.) at 750 °C under a 100 mTorr oxygen pressure. Stoichiometric polycrystalline HZO and LSMO targets, both synthesized by conventional solid-state reaction, were ablated by a pulsed output of 248 nm wavelength from a PLD20 KrF excimer laser (Excimer, China) with a laser fluence of 1.5 J/cm² and a repetition rate of 2 Hz. The HZO and LSMO layer thickness was controlled using their respective deposition rate calibrated by fitting the X-ray reflection (XRR) data through GenX software. HZO/SrTiO₃ (HZO/STO) superlattices, i.e., replacing the 1-nm LSMO layers with 1-nm STO layers, were also deposited for comparison. Hereafter, the superlattices are labeled as (HZO/LSMO)_{*n*} or (HZO/STO)_{*n*}, where *n* denotes the number of periods. Pt top electrodes with a diameter of 30 μm were deposited through a shadow mask using an AJA Orion-8-UHV sputtering system at room temperature. Ohmic contact with the LSMO electrode was achieved by silver paste. The crystal structure and thickness of the HZO, LSMO, and STO layers were examined by X-ray diffraction (XRD) and XRR using a Brucker D8 Discover diffractometer. A Helios G4 UX (Thermo Fisher) focused ion beam setup was used to prepare cross-sectional scanning transmission electron microscopy (STEM) samples. Aberration-corrected STEM imaging was acquired with a high-angle annular dark field (HAADF) detector in an FEI Titan3 G2 60–300 microscope at 300 kV. The surface morphology of the superlattices was characterized using an Asylum Research Cypher ES atomic force microscope (AFM). Ferroelectric remanent hysteresis loops and fatigue characteristics were studied using a radiant precision multiferroic system. Fatigue characteristics were measured by cycling under 50 kHz bipolar pulses of various amplitudes.

III. RESULTS AND DISCUSSION

A. Structural characterization

Figure 1(a) shows the XRD θ – 2θ patterns of HZO thin films in various thicknesses deposited on LSMO/LSAT substrates. The diffraction peak at around 30.2° is well-known and originates from the (111)-plane of *o*-HZO.

As shown in Fig. S1(a) in the Supplemental Materials [30], the Laue oscillations of the (111) peak in *o*-HZO films and the (110) peak in the LSMO electrode can be identified by fitting the experimental data. The peaks at approximately 31.6–31.7° belong to the Laue oscillations of the LSMO electrode. The HZO films were subjected to an in-plane tensile strain, as the *o*-HZO (111) peak is obviously shifted toward lower 2θ angles with increasing film thickness, indicating that the out-of-plane lattice parameter is elongated as the in-plane tensile strain relaxes. This in-plane tensile strain has previously been found essential to stabilize the *o*-phase in polycrystalline and epitaxial HfO₂-based ferroelectric films [12,13,22,28]. There is a peak around 28.3°, which can be assigned to the (111) diffraction of *m*-HZO, appearing in the XRD patterns of 15- and 20-nm-thick HZO but not in those of thinner films. The thermodynamically stable but nonpolar *m*-HZO usually appears near the surface of thick epitaxial HZO films, where the in-plane tensile strain relaxes, as observed in previous reports [21,28].

In order to prevent the formation of a *m*-phase in thick HZO films, 1-nm-thick LSMO or STO interlayers were inserted into the 10-nm-thick HZO layers to form (HZO/LSMO)_{*n*} or (HZO/STO)_{*n*} superlattices. It has been well-established in atomic layer deposited polycrystalline HZO thin films that a spacer layer is favorable to prevent the *m*-phase in thick films [29]. Indeed, there are no diffractions from the *m*-phase detected in the pattern of the (HZO/LSMO)₅ superlattice, although the total sample thickness is more than 50 nm, as shown in Fig. 1(b). As the number of (HZO/LSMO)_{*n*} superlattice period increases, the (111) peak from *o*-HZO obviously shifts to lower 2θ angles, indicating the expansion of lattice spacing in the out-of-plane direction and the relaxation of in-plane tensile strain in the HZO films. The (HZO/LSMO)₅ superlattice exhibits clear satellite peaks originating from the superlattice structure. As indicated by Table S1 in the Supplemental Material [30] (including Refs. [31–37]), the period of the (HZO/LSMO)₅ superlattice can be estimated to be around 10.7 nm from the satellite peaks, which is in good agreement with the nominal period. We also tried HZO/STO superlattices by replacing the LSMO layers with STO layers of the same thickness. The (HZO/STO)₅ superlattice shows a clear diffraction peak from the (111)-plane of *m*-HZO. However, the *m*-phase is almost completely suppressed in the thinner (HZO/STO)₂ superlattice, although the total thickness is still more than 20 nm. The *m*-phase already appears in HZO single-layer films with this thickness, as shown in Fig. 1(a). The LSMO or STO spacer layers interrupt the continuous HZO grain growth, as reported in HZO/Al₂O₃/HZO thin films prepared by atomic layer deposition [29]. The STO interlayers are less effective than the LSMO interlayers in suppressing the *m*-phase. The mechanism is still under investigation.

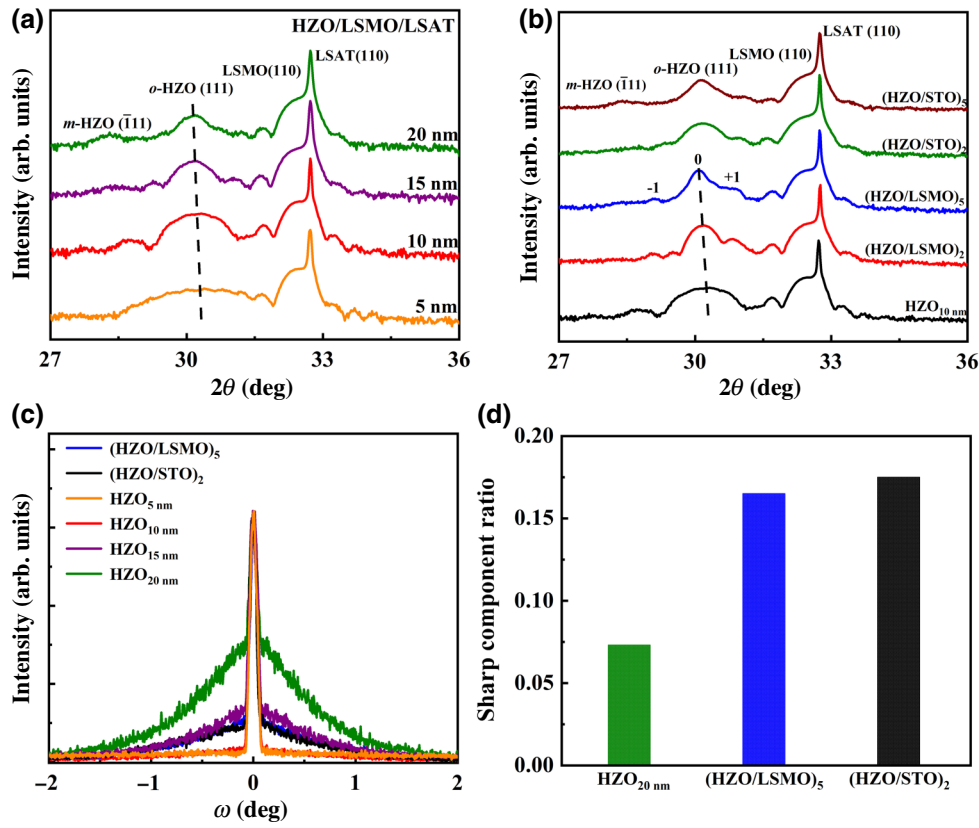


FIG. 1. XRD θ - 2θ patterns of (a) HZO films with different thicknesses and (b) (HZO/LSMO)₅, (HZO/LSMO)₂, (HZO/STO)₅, and (HZO/STO)₂ superlattices deposited on (110)-LSMO/LSAT substrates; (c) rocking curves of HZO films with different thickness, for (HZO/LSMO)₅ and (HZO/STO)₂ superlattices; (d) the sharp component ratio of 20-nm-thick HZO film, (HZO/LSMO)₅, and (HZO/STO)₂ superlattices.

Figure 1(c) shows the rocking curves of the o -HZO (111) diffraction in the (HZO/LSMO)₅, (HZO/STO)₂, and (HZO/STO)₅ superlattices in comparison with those in HZO films in various thickness. The rocking curve of the 5-nm-thick HZO film shows a full width at half maximum as small as 0.068° , indicating a well-aligned epitaxial growth. As the film thickness increases to 10 nm, a broad component appears in the rocking curve together with a sharp component. In addition, the intensity of the broad component significantly increases with increasing film thickness. The broad component demonstrates a poorly aligned mosaic growth on top of the well-aligned one [38,39], as observed previously in epitaxial HfO₂-based thin films [22,40]. Although this broad component also appears in the rocking curves of the HZO/LSMO superlattices, it is greatly suppressed by the LSMO insertion layers. Yun *et al.* proposed that the sharp:broad peak area ratio can be used to describe the overall crystallinity of the films [40]. As shown in Fig. 1(d), the insertion of the LSMO or STO layer significantly increases the intensity ratio of the sharp component. The area ratio of sharp components in the (HZO/LSMO)₅ and (HZO/STO)₂ superlattices is 2.33 and 2.44 times that of the 20-nm-thick HZO

film, respectively. This indicates that the critical thickness, above which this poorly aligned growth occurs as a method to release the accumulated elastic energy, is greatly increased by the LSMO or STO insertion layers.

The XRD ϕ -scan of the (111)-diffraction of the (HZO/LSMO)₅ superlattice is shown in Fig. 2(a), revealing six peaks with a separation $\Delta\phi = 60^\circ$, confirming the sixfold in-plane symmetry of the superlattice. This appears as a result of two domains rotated from each other by 180° with respect to the out-of-plane [111] direction, with each domain contributing to three poles, namely $(\bar{1}\bar{1}1)$, $(1\bar{1}\bar{1})$, and $(\bar{1}1\bar{1})$, separated by $\Delta\phi = 120^\circ$. Similar results were observed in doped HfO₂ thin films, as reported previously [22,28]. Figures 2(b) and 2(c) show the XRD θ - 2θ patterns of the six {111} diffractions at $\chi = 71^\circ$ with their reciprocal vectors having in-plane components compared with that of the (111) peak with its reciprocal vector completely out-of-plane for the 10-nm-thick HZO film and the (HZO/LSMO)₅ superlattice, respectively. The {111} peaks of the 10-nm-thick HZO film all appear at exactly the same Bragg angle as the out-of-plane (111) diffraction, indicating $d_{111} = d_{\bar{1}\bar{1}1} = d_{1\bar{1}\bar{1}} = d_{\bar{1}1\bar{1}} = 2.946 \text{ \AA}$, corresponding to the o -phase with the eight $\langle 111 \rangle$ reciprocal

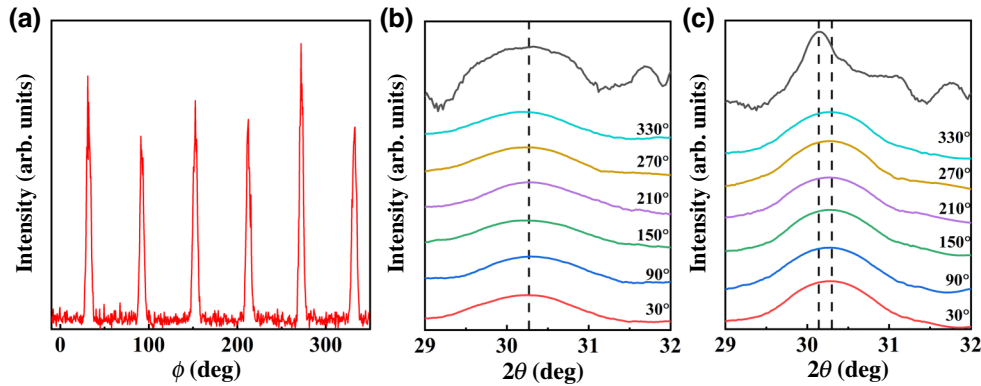


FIG. 2. (a) XRD ϕ -scan patterns of *o*-HZO (111) reflections of the (HZO/LSMO)₅ superlattice; XRD θ – 2θ patterns of the {111} peaks of the (b) 10-nm-thick HZO film and (c) the (HZO/LSMO)₅ superlattice.

vectors at the same length. However, the six peaks from the inclined {111} planes in the (HZO/LSMO)₅ superlattice all appear at a Bragg angle obviously higher than that of the (111)-plane, giving rise to a lattice spacing $d_{\bar{1}\bar{1}1} = d_{\bar{1}\bar{1}\bar{1}} = d_{11\bar{1}}$ smaller than that of the out-of-plane d_{111} , indicating a *r*-distortion by stretching the *o*-phase unit cell along the [111] direction [21,22]. This distortion can be quantified by the *r*-distortion angle δ , i.e., the deviation of the interaxial angle from 90°, assuming a rhombohedral unit cell [22]. As shown in Fig. S2 in the Supplemental Material [30], the *r*-distortion angle δ of (HZO/LSMO)₂, (HZO/STO)₂, and (HZO/LSMO)₅ superlattices, derived from lattice parameters in Fig. S2(e) in the Supplemental Material [30], increases successively, which indicates that the *r*-distortion in the (HZO/LSMO)₅ superlattice is strongest. Wei *et al.* have reported on epitaxial *r*-HZO ferroelectric films deposited on LSMO-buffered STO substrates, in which the *r*-phase was induced by a large in-plane compressive strain due to the thermal

expansion coefficient mismatch between the substrate and HZO layers [21,23]. Yun *et al.* reported that although the *r*-phase is energetically unfavorable, 5%Y:HfO₂ epitaxial thin films could be in the *Pca*₂₁ *o*-phase with a small *r*-distortion [40]. Most recently, for 5%La:HfO₂ thin films, we have reported that the strain gradient along the film's normal results in a flexoelectric field, which in turn induces a *r*-distortion in the otherwise *Pca*₂₁ *o*-phase [22]. This *r*-distortion is crucial to enhance the fatigue endurance by further stabilizing the metastable ferroelectric phase [22].

Figure 3(a) shows a cross-sectional HAADF-STEM image of the (HZO/LSMO)₅ superlattice deposited on the (110)-oriented LSMO/LSAT substrate. Different atoms can be identified since the contrast of a HAADF-STEM image scales as Z^n ($4/3 \leq n \leq 2$), where Z is the atomic number [41]. There are clearly two contrasts in the superlattice: a bright one from the relatively heavy HZO layer and a dark one from the nominal LSMO layer. Figure 3(b) shows an intensity profile in the vertical dash rectangle

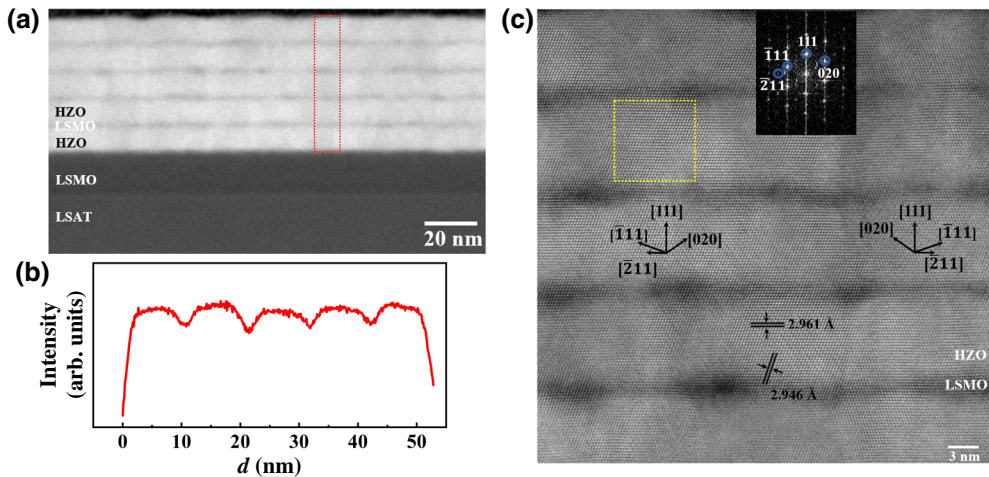


FIG. 3. (a) Cross-sectional HAADF-STEM image of the (HZO/LSMO)₅ superlattice; (b) intensity profile for the region represented by the red dashed rectangle in (a); (c) atomic resolution HAADF-STEM images of the same film observed along the [001] zone axis of the LSAT. The insets show the fast Fourier transform of the lattice, indicated by the yellow square.

in Fig. 3(a). The clear intensity oscillation indicates the superlattice structure in a periodic repetition of two component layers, 1 and 10 nm in thickness, respectively, in a period. Figure 3(c) shows a magnified HAADF-STEM image of the same superlattice observed along the [001] zone axis of LSAT. The HZO lattice shows two sets of atomic planes, one parallel to the film surface with a lattice spacing of about 2.961 Å, and the other 71° away with a lattice spacing of about 2.946 Å, in agreement with the (111) and ($\bar{1}$ 11) planes, respectively, in *o*-HZO with *r*-distortion that stretches the orthorhombic lattice along the [111] direction. Fourier transform reveals two types of domains in Fig. 3(c). The left-hand domain is in an orientation with the [111] direction pointing upper left, while the right-hand domain is in an orientation with the [$\bar{1}$ 11] direction pointing upper right. This corresponds to *o*-HZO crystal variants rotated from each other by 180° with respect to the out-of-plane [111] direction. The inset shows the fast Fourier transform within the yellow square, indicating the out-of-plane [111] direction, the [$\bar{1}$ 11] direction 71° away and the in-plane [211] direction parallel to the [1 $\bar{1}$ 0] direction of LSMO. As shown in Fig. 3(c), all the HZO layers separated by LSMO layers maintain the *o*-phase with the [111] direction out-of-plane in the absence of the *m*-HZO, as revealed by XRD.

Geometric phase analysis (GPA) and direct atomic position mappings are effective tools that show great potential for extracting complex and inhomogeneous strain distributions [42–45]. The relaxation of in-plane tensile strain in the (HZO/LSMO)₅ superlattice can also be quantified by GPA. The distributions of in-plane strain (e_{xx}) in the (HZO/LSMO)₅ superlattice, calculated relative to the average lattice parameter, are illustrated in Figs. S3(b) and S3(c) in the Supplemental Material [30]. The large local variations may originate from dislocations, which are commonly formed to relax the large in-plane strain in epitaxial films [46,47]. It is observed that e_{xx} decreases from the bottom to the top of the superlattice, which is consistent with the XRD results. The quantitative line profiles of e_{xx} are shown in Figs. S3(d) and S3(e) in the Supplemental Material [30]. The strain gradients of e_{xx} in the (HZO/LSMO)₅ superlattice are estimated above 10⁶ m⁻¹, which is similar to those reported in LaFeO₃ and BiFeO₃ epitaxial thin films [43,45]. To further prove the existence of a strain gradient in the (HZO/LSMO)₅ superlattice deposited on the LSAT substrate, the LSMO electrode was selectively etched off and the freestanding (HZO/LSMO)₅ superlattice was transferred to a Si substrate. The transferred (HZO/LSMO)₅ superlattice is expected to be free from any strain or strain gradient. Figure S4 in the Supplemental Material [30] show XRD θ –2 θ patterns of the (HZO/LSMO)₅/LSMO/LSAT heterostructure and the transferred (HZO/LSMO)₅ superlattice on Si substrate. The *o*-HZO (111) diffraction peak of the (HZO/LSMO)₅ superlattice on the LSAT substrate is asymmetric with

a clear shoulder at higher angles, indicative of a tensile strain gradient [48,49]. In contrast, the transferred (HZO/LSMO)₅ superlattice shows a symmetric *o*-HZO (111) peak due to the release of the strain.

B. Ferroelectric characteristics

Figure 4(a) shows the ferroelectric remanent hysteresis loop of the (HZO/LSMO)₅ superlattice in comparison with those of 10- and 20-nm-thick HZO films. The 20-nm-thick HZO film exhibits a small remanent polarization (P_r) of about 3.2 μC/cm², in agreement with the XRD results that nonpolar *m*-HZO coexists with ferroelectric *o*-HZO in thick films. The coercive field (E_c) values are 4.6 and 2.6 MV/cm for the 10-nm-thick HZO film and the (HZO/LSMO)₅ superlattice, respectively. According to the domain nucleation model, where the critical nucleus size of an opposite domain decreases with increasing film thickness [50,51], it is reasonable that the E_c value of the superlattice is much smaller than that of the HZO film, which is much thinner. The P_r values of the 10-nm-thick HZO film and the (HZO/LSMO)₅ superlattice are about 9.6 and 17.2 μC/cm², respectively. The current-voltage loops and leakage current curves of the 10-nm-thick HZO film and the (HZO/LSMO)₅ superlattice are shown in Fig. S5 in the Supplemental Material [30]. Moreover, the ferroelectric remanent hysteresis loops of (HZO/LSMO)₂ and (HZO/STO)₂ superlattices are shown in Fig. S6(a) in the Supplemental Material [30]. Compared with the HZO films growing on 110-oriented STO substrates [28,52], the 10-nm-thick HZO film has smaller P_r values. According to the previous reports, the HZO films deposited on the LSAT substrates have smaller remanent polarization than those on the STO substrates [53]. In addition, the P_r values obtained from the remanent hysteresis loops have a smaller value due to contributions from the leakage current being avoided. The higher P_r in the superlattice may be ascribed to the *r*-distorted *o*-phase in the superlattice. Wei *et al.* have reported that the epitaxial *r*-HZO ferroelectric films have a larger P_r compared with the *o*-HZO films [21]. The (HZO/LSMO)₅ superlattice with *r*-distortion shows a positive imprint of about 0.35 MV/cm, shifting the hysteresis loop significantly to the right. This indicates an internal electric field in the (HZO/LSMO)₅ superlattice, probably the flexoelectric field, which favors the *r*-distortion as observed in thick 5%La:HfO₂ thin films [22].

Figure 4(b) shows P_r as a function of the applied electric field (E) for the 10-nm-thick HZO film and the (HZO/LSMO)₅ superlattice. Corresponding hysteresis loops are shown in Fig. S7 in the Supplemental Material [30]. Within the applied electric field range, the P_r value of the 10-nm-thick HZO film is lower than that of the (HZO/LSMO)₅ superlattice due to its much higher E_c . With an increase in the electric field, the slope of the P_r – E curve increases when the electric field exceeds E_c , then

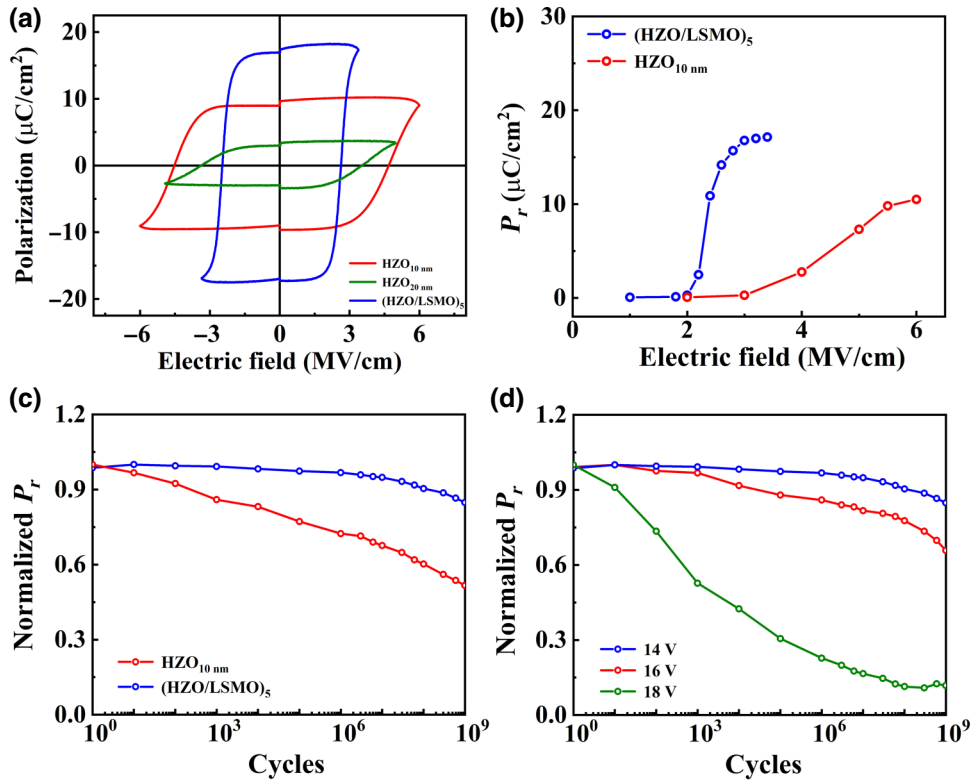


FIG. 4. (a) Ferroelectric remanent hysteresis loops of the 10- and 20-nm-thick HZO films and the (HZO/LSMO)₅ superlattice deposited on (110)-LSMO/LSAT substrates; (b) evolution of P_r with the electric field; (c) fatigue characteristics of the 10-nm HZO film and the (HZO/LSMO)₅ superlattice; and (d) fatigue characteristics of the (HZO/LSMO)₅ superlattice as functions of bipolar pulse voltages.

decreases with the saturation of polarization. The room temperature retention of polarization is shown in Fig. S8 in the Supplemental Material [30]; all these films exhibit excellent retention and maintain around 90% of the initial P_r after 10^4 s.

Figure 4(c) shows the fatigue characteristics of the HZO films represented by the normalized polarization as functions of switching cycles at room temperature. The amplitudes of the triangular cycling pulses are 5 V for the 10-nm-thick HZO film and 14 V for the (HZO/LSMO)₅ superlattice, exceeding their respective coercive fields and sufficient to saturate the polarization. The P_r of the 10-nm-thick HZO film decreases continuously with repetitive switching and only keeps 59% of its initial value after 10^9 cycles. In comparison, P_r maintains 85% of its initial value for the (HZO/LSMO)₅ superlattice after 10^9 cycles. Figure S4 in the Supplemental Material [30] shows that the P_r maintains 60% and 68% of its initial value for the (HZO/LSMO)₂ and (HZO/STO)₂ superlattices after 10^9 cycles, respectively. Fig. S9 in the Supplemental Material [30] displays positive imprint fields of (HZO/LSMO)₅ superlattice as a function of switching cycles, which nearly remains constant during the cycling. However, it is evident that stronger pulses induce larger polarization loss, about 35% and 89% reduction up to 10^9 switches, respectively,

under 16 and 18 V cycling. Corresponding hysteresis loops as a function of the number of switches are shown in Fig. S10 in the Supplemental Material [30]. Compared with the epitaxial HZO films in previous reports, which typically fatigues quickly by losing 50%–80% of polarization after 10^9 cycles [54,55], the fatigue resistance is greatly enhanced in the superlattice by inserting the LSMO layers. It has been revealed that the transition from the polar *o*-HZO to the nonpolar *m*-HZO is relevant to the fatigue [56,57]. As reported in a previous paper [22], verified via density functional theory calculations, the *o*-HZO with *r*-distortion is more stable than pure *o*-HZO. The *r*-distortion observed in La-doped HfO₂ films stabilizes the metastable *o*-phase and dramatically suppresses the fatigue [22]. Therefore, the greatly enhanced fatigue resistance observed here in the (HZO/LSMO)₅ superlattice may also be ascribed to the *r*-distortion, which occurs due to the flexoelectric effect in thick superlattice films with inevitable strain relaxation.

IV. CONCLUSION

In summary, HZO/LSMO superlattices have been deposited onto a (110)-LSMO/LSAT substrate. By inserting a 1-nm-thick LSMO spacer layer in between every

10-nm-thick HZO layers, the appearance of a *m*-phase in the thick HZO films can be greatly suppressed so that the (HZO/LSMO)₅ superlattice is free from paraelectric *m*-HZO, even though the total thickness is more than 50 nm. Here, the increased thickness inevitably leads to the relaxation of the in-plane tensile strain imposed by the substrate. The resulting strain gradient induces a *r*-distortion to the otherwise *Pca2*₁ *o*-phase with the help of the flexoelectric field, which in turn enhances the fatigue resistance by further stabilizing the metastable ferroelectric phase against the transition to the thermodynamically stable (but nonpolar) *m*-phase during the repetitive cycling. Our results provide a useful method to greatly enhance the poor fatigue resistance, which prevents integrated ferroelectric applications for HfO₂-based ferroelectric thin films.

ACKNOWLEDGMENTS

This work was sponsored by the Natural Science Foundation of China (Grants No. 52232001 and No. 12274202) and the Natural Science Foundation of Jiangsu Province, China (Grant No. BK20201246).

- [1] T. S. Böске, J. Müller, D. Bräuhaus, U. Schröder, and U. Böttger, Scale-free ferroelectricity induced by flat phonon bands in HfO₂, *Appl. Phys. Lett.* **99**, 102903 (2011).
- [2] H. Lee, M. Lee, K. Lee, J. Jo, H. Yang, Y. Kim, S. Chae, U. Waghmare, and J. Lee, Scale-free ferroelectricity induced by flat phonon bands in HfO₂, *Science* **369**, 1343 (2020).
- [3] D. Choe, S. Kim, T. Moon, S. Jo, H. Bae, S. Nam, Y. Lee, and J. Heo, Unexpectedly low barrier of ferroelectric switching in HfO₂ via topological domain walls, *Mater. Today* **50**, 8 (2021).
- [4] U. Schroeder, M. H. Park, T. Mikolajick, and C. S. Hwang, The fundamentals and applications of ferroelectric HfO₂, *Nat. Rev. Mater.* **7**, 653 (2022).
- [5] Jiachen Li, He Wang, Xinzhe Du, Zhen Luo, Yuchen Wang, Weiping Bai, Xingsong Su, Shengchun Shen, Yuwei Yin, and Xiaoguang Li, High endurance ($>10^{12}$) via optimized polarization switching ratio for Hf_{0.5}Zr_{0.5}O₂-based FeRAM, *Appl. Phys. Lett.* **122**, 082901 (2023).
- [6] W. Banerjee, A. Kashir, and S. Kamba, Hafnium oxide (HfO₂)—a multifunctional oxide: a review on the prospect and challenges of hafnium oxide in resistive switching and ferroelectric memories, *Small* **18**, 21075 (2022).
- [7] M. M. Dahan, H. Mulaosmanovic, O. Levit, S. Dünkel, S. Beyer, and E. Yalon, Sub-nanosecond switching of Si:HfO₂ ferroelectric field-effect transistor, *Nano Lett.* **23**, 1395 (2023).
- [8] S. Jo, *et al.*, Negative differential capacitance in ultrathin ferroelectric hafnia, *Nat. Electron.* **6**, 390 (2023).
- [9] H. Yoong, H. Wu, J. Zhao, H. Wang, R. Guo, J. Xiao, B. Zhang, P. Yang, S. Pennycook, N. Deng, X. Yan, and J. Chen, Epitaxial ferroelectric Hf_{0.5}Zr_{0.5}O₂ thin films and their implementations in memristors for brain-inspired computing, *Adv. Funct. Mater.* **28**, 1806037 (2018).
- [10] S. Shi, H. Xi, T. Cao, W. Lin, Z. Liu, J. Niu, D. Lan, C. Zhou, J. Cao, H. Su, T. Zhao, P. Yang, Y. Zhu, X. Yan, E. Y. Tsymbal, H. Tian, and J. Chen, Interface-engineered ferroelectricity of epitaxial Hf_{0.5}Zr_{0.5}O₂ thin films, *Nat. Commun.* **14**, 1780 (2023).
- [11] K. Katayama, T. Shimizu, O. Sakata, T. Shiraishi, S. Nakamura, T. Kiguchi, A. Akama, T. J. Konno, H. Uchida, and H. Funakubo, Orientation control and domain structure analysis of {100}-oriented epitaxial ferroelectric orthorhombic HfO₂-based thin films, *J. Appl. Phys.* **119**, 134101 (2016).
- [12] T. Shiraishi, K. Katayama, T. Yokouchi, T. Shimizu, T. Oikawa, O. Sakata, H. Uchida, Y. Imai, T. Kiguchi, T. Konno, and H. Funakubo, Impact of mechanical stress on ferroelectricity in (Hf_{0.5}Zr_{0.5})O₂ thin films, *Appl. Phys. Lett.* **108**, 262904 (2016).
- [13] M. Park, H. Kim, Y. Kim, T. Moon, and C. Hwang, The effects of crystallographic orientation and strain of thin Hf_{0.5}Zr_{0.5}O₂ film on its ferroelectricity, *Appl. Phys. Lett.* **104**, 072901 (2014).
- [14] S. Mueller, J. Mueller, A. Singh, S. Riedel, J. Sundqvist, U. Schroeder, and T. Mikolajick, Incipient ferroelectricity in Al-Doped HfO₂ thin films, *Adv. Funct. Mater.* **22**, 2412 (2012).
- [15] J. Müller, T. S. Böске, U. Schröder, S. Mueller, D. Bräuhaus, U. Böttger, L. Frey, and T. Mikolajick, Ferroelectricity in simple binary ZrO₂ and HfO₂, *Nano Lett.* **12**, 4318 (2012).
- [16] U. Schroeder, C. Hwang, and H. Funakubo, *Ferroelectricity in Doped Hafnium Oxide: Materials, Properties and Devices, Woodhead Publishing Series in Electronic and Optical Materials* (Elsevier Science, New York, 2019).
- [17] S. Starschich, D. Griesche, T. Schneller, R. Waser, and U. Böttger, Chemical solution deposition of ferroelectric yttrium-doped hafnium oxide films on platinum electrodes, *Appl. Phys. Lett.* **104**, 202903 (2014).
- [18] T. Shiraishi, S. Choi, T. Kiguchi, and T. J. Konno, Structural evolution of epitaxial CeO₂-HfO₂ thin films using atomic-scale observation: Formation of ferroelectric phase and domain structure, *Acta Mater.* **235**, 118091 (2022).
- [19] M. H. Park, Y. H. Lee, H. J. Kim, Y. J. Kim, T. Moon, K. D. Kim, J. Müller, A. Kersch, U. Schroeder, T. Mikolajick, and C. S. Hwang, Ferroelectricity and antiferroelectricity of doped thin HfO₂-based films, *Adv. Mater.* **27**, 1811 (2015).
- [20] M. H. Park, Y. H. Lee, H. J. Kim, Y. J. Kim, T. Moon, K. D. Kim, S. D. Hyun, T. Mikolajick, U. Schroeder, and C. S. Hwang, Understanding the formation of the metastable ferroelectric phase in hafnia-zirconia solid solution thin films, *Nanoscale* **10**, 716 (2018).
- [21] Y. Wei, P. Nukala, M. Salverda, S. Matzen, H. J. Zhao, J. Momand, A. Everhardt, G. R. Blake, P. Lecoer, B. J. Kooi, J. Íñiguez, B. Dkhil, and B. Noheda, A rhombohedral ferroelectric phase in epitaxially strained Hf_{0.5}Zr_{0.5}O₂ thin films, *Nat. Mater.* **17**, 1095 (2018).
- [22] P. Jiao, H. Cheng, J. Li, H. Chen, Z. Liu, Z. Xi, W. Ding, X. Ma, J. Wang, N. Zheng, Y. Nie, Y. Deng, L. Bellaiche, Y. Yang, and D. Wu, Flexoelectricity-stabilized ferroelectric phase with enhanced reliability in ultrathin La:HfO₂ films, *Appl. Phys. Rev.* **10**, 031417 (2023).
- [23] P. Nukala, Y. Wei, V. Haas, Q. Guo, J. Antoja-Lleonart, and B. Noheda, Guidelines for the stabilization of a polar

- rhombohedral phase in epitaxial $\text{Hf}_{0.5}\text{Zr}_{0.5}\text{O}_2$ thin films, *Ferroelectrics* **569**, 148 (2020).
- [24] I. Fina and F. Sánchez, Epitaxial ferroelectric HfO_2 films: growth, properties, and devices, *ACS Appl. Electron. Mater.* **3**, 1530 (2021).
- [25] J. Lyu, I. Fina, R. Solanas, J. Fontcuberta, and F. Sánchez, Robust ferroelectricity in epitaxial $\text{Hf}_{1/2}\text{Zr}_{1/2}\text{O}_2$ thin films, *Appl. Phys. Lett.* **113**, 082902 (2018).
- [26] M. Shandalova and P. C. McIntyre, Size-dependent polymorphism in HfO_2 nanotubes and nanoscale thin films, *J. Appl. Phys.* **106**, 084322 (2009).
- [27] H. Cheng, P. Jiao, J. Wang, M. Qing, Y. Deng, J. Liu, L. Bellaiche, D. Wu, and Y. Yang, Tunable and parabolic piezoelectricity in hafnia under epitaxial strain, *Nat. Commun.* **15**, 394 (2024).
- [28] P. Jiao, J. Li, Z. Xi, X. Zhang, J. Wang, Y. Yang, Y. Deng, and D. Wu, Ferroelectric $\text{Hf}_{0.5}\text{Zr}_{0.5}\text{O}_2$ thin films deposited epitaxially on (110)-oriented SrTiO_3 , *Appl. Phys. Lett.* **119**, 252901 (2021).
- [29] H. J. Kim, M. H. Park, Y. J. Kim, Y. H. Lee, W. Jeon, T. Gwon, T. Moon, K. Do Kim, and C. S. Hwang, Grain size engineering for ferroelectric $\text{Hf}_{0.5}\text{Zr}_{0.5}\text{O}_2$ films by an insertion of Al_2O_3 interlayer, *Appl. Phys. Lett.* **105**, 192903 (2014).
- [30] See the Supplemental Material at <http://link.aps.org/supplemental/10.1103/PhysRevApplied.21.054024> for more details of the structural and ferroelectric characterizations.
- [31] A. H. Eltoukhy and J. E. Greene, Compositionally modulated sputtered InSb/GaSb superlattices: Crystal growth and interlayer diffusion, *J. Appl. Phys.* **50**, 1 (1979).
- [32] T. Song, R. Bachelet, G. Saint-Girons, R. Solanas, I. Fina, and F. Sánchez, Epitaxial ferroelectric La-doped $\text{Hf}_{0.5}\text{Zr}_{0.5}\text{O}_2$ thin films, *ACS Appl. Electron. Mater.* **2**, 3221 (2020).
- [33] D. Pesquera, X. Martí, V. Holy, R. Bachelet, G. Herranz, and J. Fontcuberta, X-ray interference effects on the determination of structural data in ultrathin $\text{La}_{2/3}\text{Sr}_{1/3}\text{MnO}_3$ epitaxial thin films, *Appl. Phys. Lett.* **99**, 221901 (2011).
- [34] D. B. McWhan, M. Gurvitch, J. M. Rowell, and L. R. Walker, Structure and coherence of NbAI multilayer films, *J. Appl. Phys.* **54**, 3886 (1983).
- [35] I. Jaakola, J. Levoska, and M. Tyunina, Multilayers and superlattices of ferroelectric barium strontium titanate, *J. Appl. Phys.* **102**, 014108 (2007).
- [36] Y. Lu, J. Klein, F. Herbstritt, J. B. Philipp, A. Marx, L. Alff, R. Gross, and H. Zhang, Structure and transport properties of coherently strained $\text{La}_{2/3}\text{Ca}_{1/3}\text{MnO}_3/\text{SrTiO}_3$ superlattices, *Phys. Status Solidi B* **242**, 1545 (2005).
- [37] P. F. Micell, D. A. Neumann, and H. Zabel, X-ray refractive index: A tool to determine the average composition in multilayer structures, *Appl. Phys. Lett.* **48**, 24 (1986).
- [38] S. Park, T. S. Cho, S. J. Doh, J. L. Lee, and J. H. Je, Structural evolution of ZnO /sapphire (001) heteroepitaxy studied by real time synchrotron x-ray scattering, *Appl. Phys. Lett.* **77**, 3 (2000).
- [39] B. Voigtländer and A. Zinner, Simultaneous molecular beam epitaxy growth and scanning tunneling microscopy imaging during Ge/Si epitaxy, *Appl. Phys. Lett.* **63**, 3055 (1993).
- [40] Y. Yun, P. Buragohain, M. Li, Z. Ahmadi, Y. Zhang, X. Li, H. Wang, J. Li, P. Lu, L. Tao, H. Wang, J. E. Shield, E. Y. Tsymbal, A. Gruverman, and X. Xu, Intrinsic ferroelectricity in Y-doped HfO_2 thin films, *Nat. Mater.* **21**, 903 (2022).
- [41] M. Treacy, Z dependence of electron scattering by single atoms into annular dark-field detectors, *Microsc. Microanal.* **17**, 847 (2011).
- [42] G. Catalan, A. Lubk, A. H. G. Vlooswijk, E. Snoeck, C. Magen, A. Janssens, G. Rispens, G. Rijnders, D. H. A. Blank, and B. Noheda, Flexoelectric rotation of polarization in ferroelectric thin films, *Nat. Mater.* **10**, 963 (2011).
- [43] Y. L. Tang, Y. L. Zhu, Y. Liu, Y. J. Wang, and X. L. Ma, Giant linear strain gradient with extremely low elastic energy in a perovskite nanostructure array, *Nat. Commun.* **8**, 15994 (2017).
- [44] Y. L. Tang, Y. L. Zhu, X. L. Ma, A. Y. Borisevich, A. N. Morozovska, E. A. Eliseev, W. Y. Wang, Y. J. Wang, Y. B. Xu, Z. D. Zhang, and S. J. Pennycook, Observation of a periodic array of flux-closure quadrants in strained ferroelectric PbTiO_3 films, *Science* **348**, 547 (2015).
- [45] M. Wu, Z. Jiang, X. Lou, F. Zhang, D. Song, S. Ning, M. Guo, S. J. Pennycook, J. Dai, and Z. Wen, Flexoelectric thin-film photodetectors, *Nano Lett.* **21**, 2946 (2021).
- [46] A. P. Payne, W. D. Nix, B. M. Lairson, and B. M. Clemens, Strain relaxation in ultrathin films: A modified theory of misfit-dislocation energetics, *Phys. Rev. B* **47**, 13730 (1993).
- [47] M. X. Wang, F. J. Xu, N. Xie, Y. H. Sun, B. Y. Liu, W. K. Ge, X. N. Kang, Z. X. Qin, X. L. Yang, X. Q. Wang, and B. Shen, High-temperature annealing induced evolution of strain in AlN epitaxial films grown on sapphire substrates, *Appl. Phys. Lett.* **114**, 112105 (2019).
- [48] E. Bellet-Amalric, C. Adelmann, E. Sarigiannidou, J. L. Rouvière, G. Feuillet, E. Monroy, and B. Daudin, Plastic strain relaxation of nitride heterostructures, *J. Appl. Phys.* **95**, 1127 (2004).
- [49] D. Lee, A. Yoon, S. Y. Jang, J.-G. Yoon, J.-S. Chung, M. Kim, J. F. Scott, and T. W. Noh, Giant flexoelectric effect in ferroelectric epitaxial thin films, *Phys. Rev. Lett.* **107**, 057602 (2011).
- [50] H. F. Kay and J. W. Dunn, Thickness dependence of the nucleation field of triglycine sulphate, *Philos. Mag.* **7**, 2027 (1962).
- [51] S. Migita, H. Ota, H. Yamada, K. Shibuya, A. Sawa, and A. Toriumi, Polarization switching behavior of Hf-Zr-O ferroelectric ultrathin films studied through coercive field characteristics, *Jpn. J. Appl. Phys.* **57**, 04FB01 (2018).
- [52] T. Song, H. Tan, S. Estandía, J. Gàzquez, M. Gich, N. Dix, I. Fina, and F. Sánchez, Improved polarization and endurance in ferroelectric $\text{Hf}_{0.5}\text{Zr}_{0.5}\text{O}_2$ films on $\text{SrTiO}_3(110)$, *Nanoscale* **14**, 2337 (2022).
- [53] K. Liu, F. Jin, X. Zhang, K. Liu, Z. Zhang, E. Hua, J. Zhang, H. Ye, G. Gao, C. Ma, L. Wang, and W. Wu, Anisotropic strain-mediated symmetry engineering and enhancement of ferroelectricity in $\text{Hf}_{0.5}\text{Zr}_{0.5}\text{O}_2/\text{La}_{0.67}\text{Sr}_{0.33}\text{MnO}_3$ heterostructures, *Adv. Funct. Mater.* **33**, 2209925 (2022).
- [54] T. Song, R. Bachelet, G. Saint-Girons, I. Fina, and F. Sanchez, Ferroelectric $\text{Hf}_{0.5}\text{Zr}_{0.5}\text{O}_2$ films with improved

- endurance obtained through low temperature epitaxial growth on seed layers, *Nanoscale* **15**, 5293 (2023).
- [55] J. Lyu, T. Song, I. Fina, and F. Sánchez, High polarization, endurance and retention in sub-5 nm $\text{Hf}_{0.5}\text{Zr}_{0.5}\text{O}_2$ films, *Nanoscale* **12**, 11280 (2020).
- [56] S. S. Fields, S. W. Smith, P. J. Ryan, S. T. Jaszewski, I. A. Brummel, A. Salanova, G. Esteves, S. L. Wolfley, M. D. Henry, P. S. Davids, and J. F. Ihlefeld, Phase-exchange-driven wake-up and fatigue in ferroelectric hafnium zirconium oxide films, *ACS Appl. Mater. Interfaces* **12**, 26577 (2020).
- [57] J. Yuan, G. Mao, K. Xue, N. Bai, C. Wang, Y. Cheng, H. Lyu, H. Sun, X. Wang, and X. Miao, Ferroelectricity in HfO_2 from a coordination number perspective, *Chem. Mater.* **35**, 94 (2023).